

Entropic Stabilization and Descriptors of Structural Transformation in High Entropy Alloys

Narendra Kumar^{1,2} and Umesh V. Waghmare^{2,*}

¹*Chemistry and Physics of Materials Unit, Jawaharlal Nehru Centre for Advanced Scientific Research (JNCASR), Bangalore, India - 560064*

²*Theoretical Sciences Unit, Jawaharlal Nehru Centre for Advanced Scientific Research (JNCASR), Bangalore, India - 560064*

With first-principles theoretical analysis of the local structure using Bond Orientational Order parameters and Voronoi partitioning, we establish (a) HCP→BCC structural transformation in high-entropy alloys (HEAs) $\text{Nb}_x(\text{HfZrTi})_y$ at 16% Nb-concentration, and (b) that the internal lattice distortions (ILDs) peak at the transition. We demonstrate that the relative stability of HCP and BCC structures is driven by energetics, while the overall stability is achieved with contribution from the vibrational entropy that exceeds the configurational entropy of mixing. We show that along with atomic size mismatch, low average number (< 5) of valence electrons and disparity in the crystal structures of constituent elements are responsible for larger ILDs in $\text{Nb}_x(\text{HfZrTi})_y$ than in HEAs like $\text{Nb}_a\text{Mo}_b\text{W}_c\text{Ta}_d$.

I. INTRODUCTION

Alloying has been central to the progress of human civilization since the Bronze age. In conventional alloys, small amounts of secondary elements are mixed with primary ones. The resulting alloy is named based on the primary element like ferrous, aluminum, copper, and nickel alloys. The last two decades^{1–7} have witnessed an unconventional method of alloy design with equiatomic mixing of four or more elements. Stability of such alloy is assumed to be dominated by configurational entropic contributions, and hence they are named high-entropy alloys (HEAs). Beginning with the work of Yeh et al.¹ and Cantor et al.², HEAs have stimulated intense research to develop understanding of their phase stability and superb mechanical behavior^{3–6,8}.

Four *core effects*⁹ govern the stability and behavior of HEAs: 1) high configurational entropy of mixing attributed to stabilizing solid solution phase, 2) severe lattice distortions due to mismatch in the chemistry of alloying elements, 3) sluggish diffusion kinetics, and 4) the cocktail effect resulting in extraordinary properties. While the enhanced configurational entropy lowers the Gibbs free energy, it is not the sole factor responsible for forming a single-phase (if at all) solid-solution^{10–12} in preference to competing phases such as intermetallics, precipitates, multiphase, and amorphous structures^{13–15}. It is implicitly evident from the existence of limited single-phase solid-solution HEAs.

According to Hume-Rothery rules¹⁶, a substitutional solid-solution forms if the constituent mixing elements have similar atomic sizes (radii difference $\leq 15\%$), electronegativities, valencies, and the same crystal structure. Generally, HEAs do not satisfy all of these rules¹⁷, and therefore, deviations from the ideal lattice structure are seen. These structural deviations, termed internal lattice distortions (ILDs), are the combined effect of the size mismatch, differences in constituent elemental crystal structures and their valencies, and bond-heterogeneities among mixing elements.

In this work, we demonstrate that the BCC structure of $\text{Nb}_x(\text{HfZrTi})_y$ gets stabilized with increasing Nb-concentration, marking an HCP→BCC transition. We show that the associated structural changes and variation in average number of valence electrons with the addition of Nb result in large fluctuations in ILDs. Through comparative analysis of Gibbs free energy of quaternary HEAs $\text{Nb}_x(\text{HfZrTi})_y$ and $\text{Nb}_a\text{Mo}_b\text{W}_c\text{Ta}_d$, we find that the entropy stabilizes the former while the enthalpy of formation ensures the stability of the latter.

II. COMPUTATIONAL DETAILS

We use special quasirandom structures (SQS)^{18–20} of HEAs to approximately model their chemical disorder. For each alloy, we generate SQS with $3 \times 3 \times 2$ periodic supercell (36 atoms) of the conventional unit cells of BCC or HCP structures (see SI section I. for SQS details). We considered BCC and HCP host lattices of $\text{Nb}_x(\text{HfZrTi})_y$ alloys and only the BCC lattice of $\text{Nb}_a\text{Mo}_b\text{W}_c\text{Ta}_d$. As the reference ideal solid solution for comparison, we chose SQS of completely miscible BCC Mo_pW_q alloys for which the heat of mixing at any composition vanishes^{21,22}. Lattice parameters of SQS configurations were estimated using Vegard's law²³, which were optimized through structural relaxation to an energy minimum.

We perform full structural relaxation of these model SQS within the density functional theory (DFT) methods incorporated in the Quantum ESPRESSO package²⁴. We used a generalized gradient approximation (GGA)²⁵ and Perdew-Burke-Ernzerhof²⁶ functional of electronic exchange-correlation energy. We employ projector augmented wave potentials²⁷ and represent the electronic wave functions and charge density with plane wave basis sets truncated at energy cutoffs of 60 Ry and 500 Ry respectively. Uniform meshes of $3 \times 3 \times 4$ and $3 \times 3 \times 3$ k -points were used in sampling integrations over Brillouin zones of BCC and HCP-based supercells respectively. Using Hellman-Feynman forces

and Broyden Fletcher Goldfarb Shanno (BFGS) scheme, each alloy SQS is relaxed till the force components on each atom \vec{F} becomes less than 10^{-3} Ry/Bohr. Total energy was converged within 10^{-8} Ry to achieve electronic self-consistency. Fermi-Dirac distribution with a width of $k_B T = 0.002$ Ry is used for smoothening the discontinuity in occupation numbers of electronic states.

We use the Debye model to estimate vibrational entropy. The Debye temperature (θ_D) of each alloy SQS was extracted from their elastic moduli matrix obtained from the thermo_pw package²⁸. θ_D is used as a single parameter within Debye model to estimate the vibrational entropy of each alloy.

To analyze the local structure of relaxed SQS lattices of HEAs, we investigate (a) the nearest-neighbor bond alignments of each atom through bond-orientational order parameters using a recently developed python library *pyscal*²⁹, and (b) geometric features of the Voronoi cell constructed around each atom using *Voro++* library³⁰ for Voronoi analysis.

III. RESULTS AND DISCUSSION

Our motivation for analysis of the relative stability of BCC and HCP structures of $\text{Nb}_x(\text{HfZrTi})_y$ comes from the distinct crystal structures taken by its constituent elements at ambient conditions: Nb occurs in BCC structure, and Hf, Zr, and Ti occur in HCP structure. Secondly, Hf, Zr, and Ti undergo structural transformation to BCC structure at high temperature from their stable low-temperature HCP structure³¹. Experimentally, the equiatomic NbHfZrTi alloy occurs in the BCC structure³²⁻³⁴. Our calculations (Fig. 1(a)) also support this as we find that at equiatomic and higher Nb-concentrations, SQS of $\text{Nb}_x(\text{HfZrTi})_y$ of BCC lattice is more stable than that of HCP lattice. We find this structural preference in randomized structural models as well. With increasing Nb-concentration, Zhang et al.³⁵ report ω ($P6/mmm$) \rightarrow BCC transformation rather than HCP ($P6_3/mmc$) \rightarrow BCC, which poses the question of the structure of low Nb-concentration $\text{Nb}_x(\text{HfZrTi})_y$ alloys. To address this, we simulated a few SQS models of $(\text{HfZrTi})_{12}$ considering HCP and ω lattices, and found that SQS on the HCP lattices were more stable than those on the ω ones (see SI Table I. and SI Fig. 3) by more than 15 meV/atom. Thus, we analyze here HCP to BCC transformation.

In Fig. 1(a), we report a structural transformation equiatomic composition of $\text{Nb}_x(\text{HfZrTi})_y$ based on the relative DFT energies of SQS corresponding to HCP and BCC lattices. We find significant changes in the atomic positions of relaxed SQS from their ideal lattice structure; thus, ILDs help lower the energy. As these atomic displacements developed during relaxation severely distort the ideal lattice, we require local structural descriptors to ascertain the true phase of relaxed HEAs. At nonzero temperature,

any crystalline material exhibits dynamic ILDs due to thermal vibrations. However, static ILDs are present in HEAs even at $T = 0$ K due to differences among their atomic constituents. In a recent study³⁶, root mean squared displacement of atoms in BCC structure of NbHfZrTi at $T = 0$ K was estimated at 9% of its lattice parameter. Such large ILDs make identification of the lattice structure challenging. Experimentally, XRD gives the average crystalline structure with Bragg peaks broadened due to ILDs.

A. Local structure and identification of the underlying lattice

a. (a) Voronoi analysis To examine the local structure at the atomic scale, we first use Voronoi decomposition involving the construction of a polyhedron around each lattice point (atomic site) known as Voronoi cell (or Wigner-Seitz cell in crystallography). Since the atomic radii of constituent atoms in HEAs are similar, we treated each atom as a point particle in Voronoi decomposition. The Voronoi cell of a BCC lattice point is a *truncated octahedron* (see Fig. 1(d)) that has 6 square and 8 hexagonal faces. The Voronoi cell of an HCP lattice point is a *trapezo-rhombic dodecahedron* (see Fig. 1(e)) that has 6 trapezium- and 6 rhombus-shaped faces. The order of a vertex in a graph is the number of edges incident into it. Each Voronoi vertex of a BCC lattice is of order 3, which is topologically stable (**type-A**). In contrast, some Voronoi vertices of the HCP lattice are of order 4, which are topologically unstable (**type-B**). With a slight perturbation, topologically unstable vertices modify the Voronoi cell characteristics by creating new faces³⁷. We demonstrate this for supercell of BCC and HCP lattices by adding random displacements to the positions of their lattice points. While the Voronoi cells of the BCC lattice does not evolve to have any new polygonal faces, pentagonal and hexagonal faces appear in the Voronoi polyhedra of randomly perturbed HCP lattice originating at the unstable vertices of order 4 (see SI Fig. 2(b)).

We use this feature of geometric instability of Voronoi vertices to identify BCC and HCP lattices of minimum energy SQS of $\text{Nb}_x(\text{HfZrTi})_y$ alloys (see Table contained in Fig. 1), which exhibit significant ILDs. Voronoi's with only quadrilaterals and hexagonal faces reveal that alloys with significant Nb-concentration ($x \geq 6$) optimize to a BCC lattice structure. We claim that at low Nb-concentration ($x = 0$ and 3), SQS optimize to HCP-based structures where pentagonal and hexagonal Voronoi faces originate at **type-B** Voronoi vertices due to ILDs.

b. (b) Bond-orientational order parameters We chose another class of structural descriptors called bond-orientational order parameters to confirm our claim of structural transition. The local bond-orientational order parameters (q_l) proposed by Steinhardt³⁸ capture

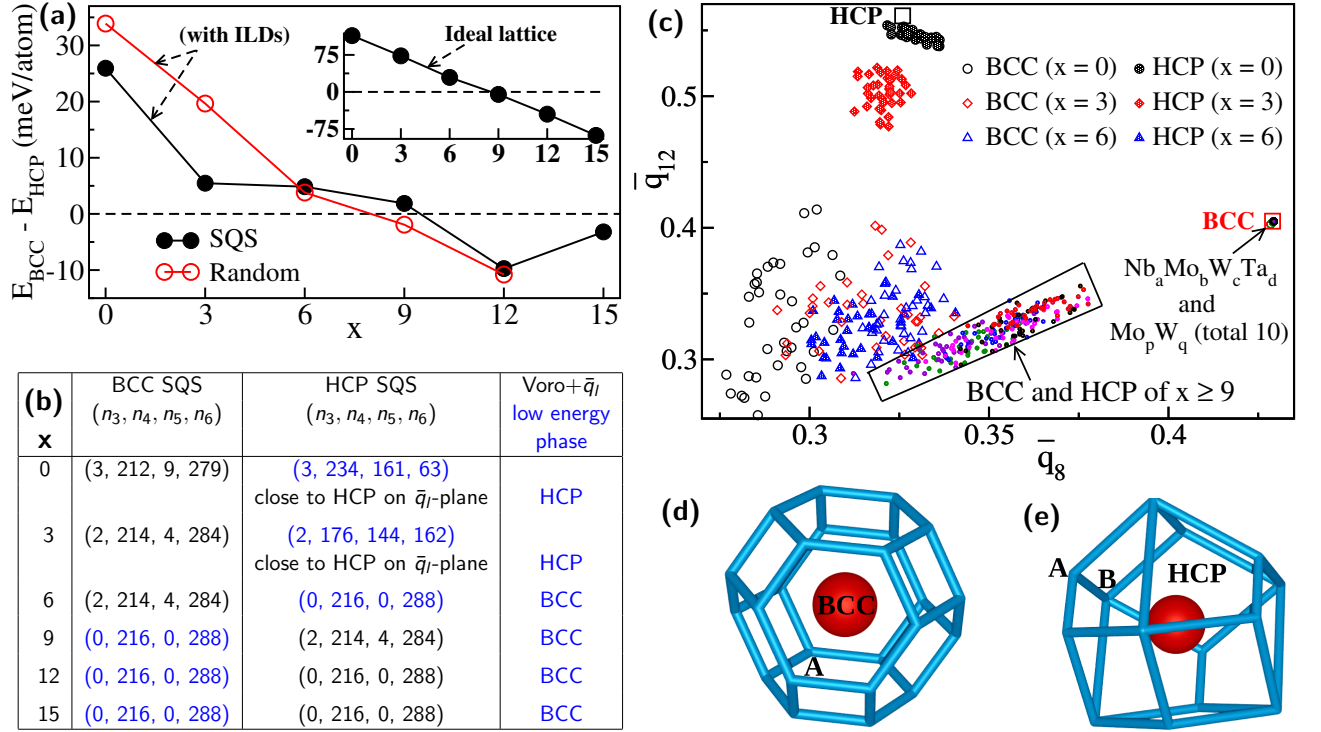


FIG. 1: Structural transition in $\text{Nb}_x(\text{HfZrTi})_y$ with $x + 3y = 36$ and analysis with Voronoi tessellation (b) and bond orientational order parameters (c). In (a), relative energies of relaxed special quasirandom and randomized HCP and BCC structures of $\text{Nb}_x(\text{HfZrTi})_y$ reveal stabilization of the BCC phase beyond 25% Nb concentration (i.e; $x \geq 9$), corresponding to equiatomic composition. Unrelaxed SQS with ideal lattice (inset) also reveals the same. In (b), n_k is the the number of k -sided Voronoi faces. Voronoi cell of an ideal BCC lattice point has squares and hexagons (d), while that of an HCP lattice point has only quadrilaterals (e). Voronoi vertex of order 3 (type-A) is stable and robust against internal lattice distortions (ILDs), while of the higher order (type-B) is unstable as new polygons appear there under distortion (see SI Fig. 1). From the Voronoi faces analysis (b) of energetically favorable SQS configurations as seen in (a), we find that a distorted BCC structure of $\text{Nb}_x(\text{HfZrTi})_y$ is stabilized for $x \geq 6$, corresponding to 16% Nb-concentration rather than equiatomic concentration. (c) The plane of bond orientational parameters (\bar{q}_8, \bar{q}_{12}) facilitates identification of the lattice structure having low ILDs. It is clear that structures of $\text{Nb}_a\text{Mo}_b\text{W}_c\text{Ta}_d$ and Mo_pW_q optimize to perfect BCC lattice with not much ILDs while $\text{Nb}_x(\text{HfZrTi})_y$ exhibit severe ILDs as evident in a wide spread in their \bar{q}_l values. The HCP SQS of low Nb-concentration ($x = 0$ and 3) allows optimize to points rather close to that of perfect HCP lattice on (\bar{q}_8, \bar{q}_{12}) plane. Thus we identify HCP→BCC transition in $\text{Nb}_x(\text{HfZrTi})_y$ at 16% Nb-concentration.

the signatures of local structure. For each atom, q_l is written in terms of spherical harmonics of θ_{ij} and ϕ_{ij} of orientational unit bond vectors joining neighboring sites i and j :

$$q_{lm}(i) = \frac{1}{n(i)} \sum_{j=1}^{n(i)} Y_{lm}(\theta_{ij}, \phi_{ij})$$

$$q_l(i) = \sqrt{\frac{4\pi}{2l+1} \sum_{m=-l}^l |q_{lm}(i)|^2}, \quad (1)$$

where $n(i)$ is the number of neighbor atoms around i^{th} atom.

These local bond-orientational parameters are ultra-sensitive to the symmetry of the crystal and help

identify simple phases such as BCC, FCC, and HCP. For different ideal crystals, q_l values are distinct except for q_l of odd l (see SI Table II). ILDs or thermal noise disturb the crystal's local structure symmetry, and result in changes in q_l values and complicate the identification of the average lattice structure. Lechner and Dellago³⁹ showed that locally averaged \bar{q}_l s:

$$\bar{q}_{lm}(i) = \frac{1}{n(i)} \sum_{k=0}^{n(i)} q_{lm}(k)$$

$$\bar{q}_l(i) = \sqrt{\frac{4\pi}{2l+1} \sum_{m=-l}^l |\bar{q}_{lm}(i)|^2}, \quad (2)$$

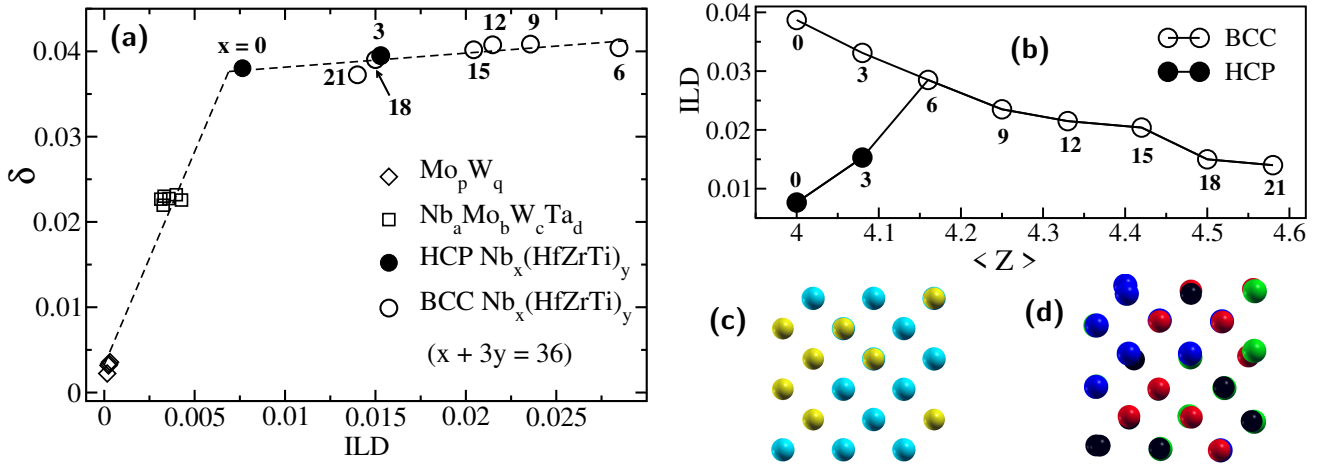


FIG. 2: Factors of ILDs: (a) In binary Mo_pW_q (four different compositions), quaternary $\text{Nb}_a\text{Mo}_b\text{W}_c\text{Ta}_d$ (six different compositions), and $\text{Nb}_x(\text{HfZrTi})_y$ (x is written near the symbols) alloys, internal lattice distortions (ILDs) are of the order of 10^{-4} , 10^{-3} , and 10^{-2} respectively. The z -axis view of relaxed SQS of MoW (c) and NbHfZrTi (d) show significant presence of ILDs in the latter. Although atomic size mismatch (δ) is a primary factor of ILDs, the significant variation in ILDs across different compositions of $\text{Nb}_x(\text{HfZrTi})_y$ without any remarkable change in their δ values asks for another possible factor. In contrast to HEAs $\text{Nb}_a\text{Mo}_b\text{W}_c\text{Ta}_d$, the structural differences among the constituent elements of $\text{Nb}_x(\text{HfZrTi})_y$ and associated HCP \rightarrow BCC transition at $x = 6$ where ILDs also peak (b) explains for the variation in their ILDs. For BCC lattice SQS, ILDs decrease with increase in average valency ($\langle Z \rangle$) and that occurs when Nb-concentration (x) increases.

work better in identifying the Bravais lattice of distorted crystals (see SI Fig. 4). For an ideal lattice, \bar{q}_l coincides with q_l , and the separation between the two measures the loss of structural order. In resolution of the lattice structure, here, we use $(\bar{q}_8, \bar{q}_{12})$ plane in which ideal BCC and HCP lattices are well separated at points (0.429, 0.405) and (0.317, 0.565), respectively.

In $(\bar{q}_8, \bar{q}_{12})$ plane (Fig. 1(c)), relaxed SQS of $\text{Nb}_a\text{Mo}_b\text{W}_c\text{Ta}_d$ and Mo_pW_q alloys always fall on to the point representing BCC lattice structure. In $\text{Nb}_x(\text{HfZrTi})_y$ alloys, SQS of HCP lattices with low Nb-concentration ($x = 0$ and 3) optimize to a structure that is close to the perfect HCP structure (here $c/a = 1.60$) with moderate distribution in \bar{q}_l , confirming that their relaxed lattices are distorted HCP structures. On the other hand, alloys with high Nb-concentration ($x \geq 9$) represented with SQS of BCC or HCP lattices converge upon relaxation to the same domain in $(\bar{q}_8, \bar{q}_{12})$ plane (see also SI Fig. 5), and exhibit distorted BCC structures as revealed earlier here in the Voronoi analysis in Fig. 1(b).

Thus, we have explicitly shown with local structural analysis that $\text{Nb}_x(\text{HfZrTi})_y$ alloys undergo a structural change from distorted HCP lattices (for $x = 0$, and 3) to distorted BCC lattices (for $x \geq 6$) at 16% Nb-concentration (since $100 \times 6/36 \simeq 16$). It is interesting that HCP lattice spontaneously transforms to BCC lattice through structural relaxation without having to cross any energy barrier. Secondly, this transformation has a signature in the electronic structures (see SI Fig. 8). At high Nb-concentration ($x \geq 9$), d -orbitals of Nb

dominate the electronic states near the Fermi energy, explaining how Nb is a BCC-stabilizer.

B. ILDs peak at the HCP to BCC transition

Wide distribution of \bar{q}_l (Fig. 1(c)) reflects on the presence of significant ILDs in HEAs $\text{Nb}_x(\text{HfZrTi})_y$. For a quantitative measure of ILDs, we use⁴⁰

$$\text{ILD} = \frac{1}{N} \sum_{i=1}^N \sqrt{(x_i - x'_i)^2 + (y_i - y'_i)^2 + (z_i - z'_i)^2} \quad (3)$$

where (x_i, y_i, z_i) and (x'_i, y'_i, z'_i) are reduced coordinates of unrelaxed sites (ideal, reference lattice points) and relaxed atomic positions of the i^{th} atom, respectively and N is the total number of atoms. We note that ILDs in binary Mo_pW_q , quaternary $\text{Nb}_a\text{Mo}_b\text{W}_c\text{Ta}_d$, and $\text{Nb}_x(\text{HfZrTi})_y$ alloys are of order of 10^{-4} , 10^{-3} , and 10^{-2} , respectively (see Fig. 2(a) and SI Table IV). In contrast to BCC (MoW)₁₈ (Fig. 2(c)), a sideview of the relaxed SQS lattice of BCC (NbHfZrTi)₉ (Fig. 2(d)) shows significant atomic perturbations from their ideal lattice sites. On increasing x in $\text{Nb}_x(\text{HfZrTi})_y$, ILDs of their energetically favorable SQS first increase, reach a maximum at $x = 6$ where HCP \rightarrow BCC transformation is marked, and then decrease subsequently (see Fig. 2(b)).

ILDs in HEAs originate from various factors such as atomic size mismatch, dissimilar crystal structures, and difference in valence electrons of their constituent elements. Multi-elemental mixing always suffer from

atomic size mismatch (δ) which is quantified as¹⁰

$$\delta^2 = \sum_{i=1}^n c_i (1 - r_i/\bar{r})^2 \quad \text{with} \quad \bar{r} = \sum_{i=1}^n c_i r_i, \quad (4)$$

where n is the number of types of elements being mixed, c_i and r_i are the atomic concentration and radius of i^{th} element, and \bar{r} is the average radius. δ is considered the primary factor relevant to ILDs^{40,41}. Fig. 2(a) depicts this for BCC Mo_pW_q , $\text{Nb}_a\text{Mo}_b\text{W}_c\text{Ta}_d$, and HCP $(\text{HfZrTi})_{12}$ alloys as their ILDs linearly increase with δ . However, taking $\text{Nb}_x(\text{HfZrTi})_y$ alloys as an example, we demonstrate that rather than δ , the elemental structural differences among their constituents and their average valence electrons (Fig. 2(b)) strongly influence ILDs. An increase in the number of average valence electrons $\langle Z \rangle$ within BCC $\text{Nb}_x(\text{HfZrTi})_y$ — achieved by the gradual rise of Nb-concentration — lowers ILDs. This mechanism of control over ILDs by tuning $\langle Z \rangle$ is consistent with a recent work reported only for BCC HEAs³⁶. Therefore, ILDs of $\text{Nb}_x(\text{HfZrTi})_y$ alloys peak at the HCP \rightarrow BCC transition (see Fig. 2(b)), and thus, ILDs in these alloys exhibit a dual effect of valency and crystal structures of constituent elements. The role of crystal structures of constituents on ILDs is further highlighted by another set of quaternary HEAs, $\text{Nb}_a\text{Mo}_b\text{W}_c\text{Ta}_d$ (composed of only BCC structural elements), which does not show noticeable variation in ILDs with compositions.

C. ILDs and configurational entropy

For a qualitative measure of ILDs, we generated and relaxed 50 distinct SQS configurations for each equiatomic BCC NbHfZrTi, NbMoWTa, and MoW alloys and analyzed them with histograms of their \bar{q}_8 values and Voronoi volumes (see Fig. 3(a)). For NbHfZrTi, the distribution exhibits a very broad peak, while it is quite narrow for NbMoWTa, and MoW has a single sharp peak. The width of these peaks in distributions, similar to Bragg peak width in XRD, serves as a measure of ILDs. Thus, ILDs are negligible in MoW and notably significant in NbHfZrTi. Here, \bar{q}_8 of MoW corresponds to that of an ideal BCC structure ($\bar{q}_8 = q_8 = 0.429$).

To analyze the effects of ILDs on configurational energy of HEAs, we consider these equiatomic SQS configurations, each with a different chemical arrangement. We find that SQS configurations of HEAs span a range of energy while the configurations of a solid-solution (MoW) have almost the same energy (Fig. 3(b) inset). Lower energy SQS configurations of HEAs are more favorable, and hence this energy fluctuation signifies a departure from the *ideal* mixing condition that requires each configuration to have the same energy¹¹. Clearly, HEAs with higher ILDs display large fluctuations in their configurational energies.

From the distribution of energy of these SQS configurations, we estimate configurational entropy. If

energy of i^{th} configuration be E_i among chosen Ω_{config} configurations, then at temperature T its probability will be

$$p_i = \frac{\exp(-\beta E_i)}{\sum_1^{\Omega_{\text{config}}} \exp(-\beta E_i)} \quad (5)$$

where $\beta = 1/(k_B T)$. Configurational entropy is deduced as

$$S_{\text{config}} = -k_B \sum_{i=1}^{\Omega_{\text{config}}} p_i \ln p_i. \quad (6)$$

We note that S_{config} of NbMoWTa and NbHfZrTi rises with temperature (see Fig. 3(b)) and saturates to the Boltzmann entropy $k_B \ln \Omega_{\text{config}}$ (here, $k_B \ln 50 = 3.912k_B$ which corresponds to MoW). In the ideal mixing of n types of elements,

$$S_{\text{config}} = S_{\text{ideal}}^{\text{mix}} = -N_{\text{atom}} k_B \sum_{i=1}^n c_i \ln c_i, \quad (7)$$

where c_i is the atomic concentration of i^{th} element, and it becomes $S_{\text{config}} = N_{\text{atom}} k_B \ln n$ for the equiatomic case. The computed configurational entropy for a finite number of SQS configurations will be lower than their ideal mixing entropy (for equiatomic quaternary systems, $N_{\text{atom}} k_B \ln n = 36k_B \ln 4 = 49.90k_B \gg k_B \ln 50$), but it captures the thermal effect that the configurational entropy approaches the Boltzmann entropy as the temperature rises. It is noteworthy that before saturation, the increase in S_{config} with temperature is slower in HEAs exhibiting stronger ILDs (see Fig. 3(b)). Thus, we demonstrate that it is reasonable to approximate the configurational entropy of HEAs as the ideal mixing entropy since each configuration becomes equiprobable even at a fairly low T (such as 300 K).

D. Entropic stabilization

The postulate that high configurational entropy stabilizes the solid-solution phase of HEAs¹ has been a topic of controversy^{12,42}. Other kinds such as vibrational, electronic, and magnetic entropies can also be important to the stability of HEAs, while major contributions come from vibrational and configurational ones⁴². In HEAs $\text{Nb}_x(\text{HfZrTi})_y$, we find that vibrational entropy contributes more than the configurational one (see SI Table V) to the total entropy. We take the total entropy comprised of vibrational entropy estimated within Debye approximation and configurational entropy approximated as the entropy of ideal solid-solution mixing. In Fig. 4(top), we show that the total entropy of non equiatomic $\text{Nb}_6(\text{HfZrTi})_{10}$ is greater than that of equiatomic $(\text{NbHfZrTi})_9$ peaking at $x = 6$. It is interesting to note that $x = 6$ marks the structural

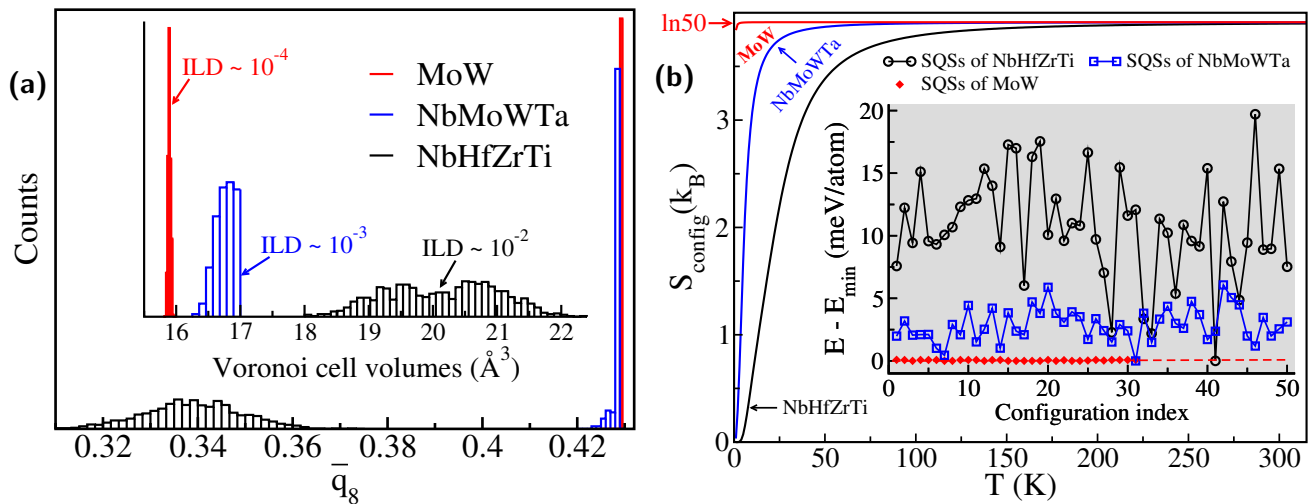


FIG. 3: Internal Lattice Distortions, energetics and configurational entropy. Histograms (a) of bond orientational parameter \bar{q}_8 and Voronoi cell volumes (inset) obtained from the relaxed structures of 50 SQS configurations of each of the equiatomic BCC alloys. A sharp peak in \bar{q}_8 of MoW marks the ideal BCC structure, a slight deviation in NbMoWTa reveals relatively weak ILDs. In contrast, notably broad and shifted peak in \bar{q}_8 of NbHfZrTi reveals its severe ILDs, and distributions of Voronoi volumes confirms this trend in ILDs and the local structure. (b) Configurational entropy approaches the entropy of ideal mixing, (Boltzmann entropy $k_B \ln 50$) at fairly low temperatures, though slower in NbHfZrTi due to larger fluctuations in the energy of their distinct SQS configurations (shown in inset) than of NbMoWTa and MoW.

transformation from HCP to BCC, where ILDs and total entropy reach their maxima.

We estimate Gibbs free energy to assess the competition between formation energy (i.e., the heat of mixing) and entropy. For the formation energy (H_f) of alloys $\text{Nb}_x(\text{HfZrTi})_y$, we subtract its concentration-weighted elemental energies in their most stable bulk crystalline phase from the energy of the alloy. The formation energy of $\text{Nb}_x(\text{HfZrTi})_y$ is positive (sign of instability) while for $\text{Nb}_a\text{Mo}_b\text{W}_c\text{Ta}_d$ it is negative (see SI Table IV and V). It means that the former is unfavorable, and the latter is favorable energetically. However, inclusion of entropy makes Gibbs free energy of formation ($H_f - TS_{\text{tot}}$) negative and stabilizes $\text{Nb}_x(\text{HfZrTi})_y$ (see Fig. 4(bottom)). For instance, H_f of $(\text{NbHfZrTi})_9$ is 0.074 eV/atom and at $T = 300$ K, alone $TS_{\text{config}} = k_B T \ln 4 = 0.036$ eV/atom is insufficient to stabilize and needed a major contribution from vibration as TS_{tot} is 0.158 eV/atom to achieve the overall stability (see SI Table V). Hence, with precise quantification, we reinforce the fundamental assumption that entropy stabilizes HEAs.

IV. CONCLUSIONS

In conclusion, we have shown that $\text{Nb}_x(\text{HfZrTi})_y$ undergoes a structural transformation from HCP to

BCC at 16% Nb-concentration. Voronoi analysis and bond-orientational order parameters are tools to help identify the average lattice structure of HEAs exhibiting large ILDs and mark this transformation. The structural differences across constituent elements and their numbers of valence electrons are dominant factors that cause ILDs in addition to atomic size mismatch in BCC HEAs. At an HCP \rightarrow BCC transition, ILDs peak and maximize the total entropy. We showed that entropy stabilizes $\text{Nb}_x(\text{HfZrTi})_y$, but with a larger share of the vibrational entropy than of the configurational entropy.

ACKNOWLEDGEMENT

NK thanks the Materials Theory Group, JNCASR, for several fruitful discussions on this work in weekly group meetings. NK also acknowledges the Council of Scientific & Industrial Research for the Ph.D. fellowship (Award No.- 09/733(0214)/2016-EMR-I). UVW acknowledges support from a JC Bose National fellowship of SERB-DST, Government of India.

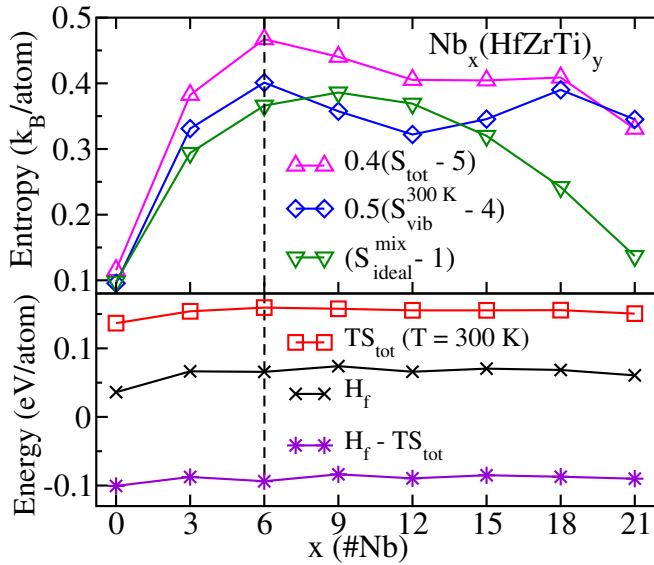


FIG. 4: Entropic stabilization of favorable phase $\text{Nb}_x(\text{HfZrTi})_y$ where $x + 3y = 36$. The total entropy comprised of Debye vibrational entropy and ideal mixing entropy reaches a maximum for BCC $\text{Nb}_6(\text{HfZrTi})_{10}$ in contrast to configurational entropy ($S_{\text{ideal}}^{\text{mix}}$) that peaks at equiatomic $(\text{NbHfZrTi})_9$ (top). Here, entropies have been scaled and shifted to facilitate comparison (see SI Table V for actual values). Entropic stabilization of $\text{Nb}_x(\text{HfZrTi})_y$ HEAs (bottom) is clear from the fact that their formation energies (H_f) are positive and entropic term, particularly with dominance of vibrational contribution (top), is needed to have favorable free energy of formation (bottom).

* waghmare@jncasr.ac.in

- ¹ J.-W. Yeh, S.-K. Chen, S.-J. Lin, J.-Y. Gan, T.-S. Chin, T.-T. Shun, C.-H. Tsau, S.-Y. Chang, Nanostructured high-entropy alloys with multiple principal elements: Novel alloy design concepts and outcomes, *Adv. Eng. Mater.* 6 (5) (2004) 299–303. doi:10.1002/adem.200300567.
- ² B. Cantor, I. Chang, P. Knight, A. Vincent, Microstructural development in equiatomic multicomponent alloys, *Mater. Sci. Eng. A* 375–377 (2004) 213–218. doi:10.1016/j.msea.2003.10.257.
- ³ Y. Zhang, T. T. Zuo, Z. Tang, M. C. Gao, K. A. Dahmen, P. K. Liaw, Z. P. Lu, Microstructures and properties of high-entropy alloys, *Progress in Materials Science* 61 (2014) 1–93. doi:10.1016/j.pmatsci.2013.10.001.
- ⁴ D. Miracle, O. Senkov, A critical review of high entropy alloys and related concepts, *Acta Mater.* 122 (2017) 448–511. doi:10.1016/j.actamat.2016.08.081.
- ⁵ S. Gorsse, M. Nguyen, O. Senkov, D. Miracle, Database on the mechanical properties of high entropy alloys and complex concentrated alloys, *Data in Brief* 21 (2018) 2664–2678. doi:10.1016/j.dib.2018.11.111.

- ⁶ E. P. George, D. Raabe, R. O. Ritchie, High-entropy alloys, *Nat. Rev. Mater.* 4 (8) (2019) 515–534. doi:10.1038/s41578-019-0121-4.
- ⁷ B. S. Murty, J.-W. Yeh, S. Ranganathan, P. Bhattacharjee, *High-entropy alloys*, Elsevier, 2019.
- ⁸ Z. Li, S. Zhao, R. O. Ritchie, M. A. Meyers, Mechanical properties of high-entropy alloys with emphasis on face-centered cubic alloys, *Progress in Materials Science* 102 (2019) 296–345. doi:10.1016/j.pmatsci.2018.12.003.
- ⁹ E. J. Pickering, N. G. Jones, High-entropy alloys: a critical assessment of their founding principles and future prospects, *Int. Mater. Rev.* 61 (3) (2016) 183–202. doi:10.1080/09506608.2016.1180020.
- ¹⁰ Y. Zhang, Y. Zhou, J. Lin, G. Chen, P. Liaw, Solid-solution phase formation rules for multi-component alloys, *Advanced Engineering Materials* 10 (6) (2008) 534–538. doi:10.1002/adem.200700240.
- ¹¹ Q. He, Y. Ye, Y. Yang, Formation of random solid solution in multicomponent alloys: from Hume-Rothery rules to entropic stabilization, *J. Phase Equilibria Diffus.* 38 (4) (2017) 416–425. doi:10.1007/s11669-017-0560-9.

- ¹² F. Otto, Y. Yang, H. Bei, E. George, Relative effects of enthalpy and entropy on the phase stability of equiatomic high-entropy alloys, *Acta Mater.* 61 (7) (2013) 2628–2638. doi:10.1016/j.actamat.2013.01.042.
- ¹³ S. Guo, C. T. Liu, Phase stability in high entropy alloys: Formation of solid-solution phase or amorphous phase, *Prog. Nat. Sci.: Mater. Int.* 21 (6) (2011) 433–446. doi:10.1016/S1002-0071(12)60080-X.
- ¹⁴ Y. Ye, Q. Wang, J. Lu, C. Liu, Y. Yang, Design of high entropy alloys: A single-parameter thermodynamic rule, *Scr. Mater.* 104 (2015) 53–55. doi:10.1016/j.scriptamat.2015.03.023.
- ¹⁵ Y. F. Ye, Q. Wang, J. Lu, C. T. Liu, Y. Yang, High-entropy alloy: challenges and prospects, *Mater. Today* 19 (6) (2016) 349–362. doi:10.1016/j.mattod.2015.11.026.
- ¹⁶ W. Hume-Rothery, R. Smallman, C. Haworth, *The structure of metals and alloys*, The Institute of Metals, London (1969).
- ¹⁷ M. C. Tropsch, J. R. Morris, M. Daene, Y. Wang, A. R. Lupini, G. M. Stocks, Beyond atomic sizes and hume-rothery rules: understanding and predicting high-entropy alloys, *Jom* 67 (10) (2015) 2350–2363. doi:10.1007/s11837-015-1594-2.
- ¹⁸ A. Zunger, S.-H. Wei, L. G. Ferreira, J. E. Bernard, Special quasirandom structures, *Phys. Rev. Lett.* 65 (1990) 353–356. doi:10.1103/PhysRevLett.65.353.
- ¹⁹ A. van de Walle, M. Asta, G. Ceder, The alloy theoretic automated toolkit: A user guide, *Calphad* 26 (4) (2002) 539–553. doi:10.1016/S0364-5916(02)80006-2.
- ²⁰ A. van de Walle, P. Tiwary, M. de Jong, D. Olmsted, M. Asta, A. Dick, D. Shin, Y. Wang, L.-Q. Chen, Z.-K. Liu, Efficient stochastic generation of special quasirandom structures, *Calphad* 42 (2013) 13–18. doi:10.1016/j.calphad.2013.06.006.
- ²¹ J. L. Murray, L. H. Bennett, H. Baker, *Binary alloy phase diagrams*, Vol. 2, ASM International (OH), 1986.
- ²² C. Colinet, A. Bessoud, A. Pasturel, Theoretical determinations of thermodynamic data and phase diagrams of BCC binary transition-metal alloys, *J. Phys. F: Met. Phys.* 18 (5) (1988) 903–921. doi:10.1088/0305-4608/18/5/010.
- ²³ A. R. Denton, N. W. Ashcroft, Vegard’s law, *Phys. Rev. A* 43 (1991) 3161–3164. doi:10.1103/PhysRevA.43.3161.
- ²⁴ P. Giannozzi, S. Baroni, N. Bonini, M. Calandra, R. Car, C. Cavazzoni, D. Ceresoli, G. L. Chiarotti, M. Cococcioni, I. Dabo, et al., Quantum espresso: a modular and open-source software project for quantum simulations of materials, *J. Phys.: Condens. Matter* 21 (39) (2009) 395502. doi:10.1088/0953-8984/21/39/395502.
- ²⁵ J. P. Perdew, J. A. Chevary, S. H. Vosko, K. A. Jackson, M. R. Pederson, D. J. Singh, C. Fiolhais, Atoms, molecules, solids, and surfaces: Applications of the generalized gradient approximation for exchange and correlation, *Phys. Rev. B* 46 (1992) 6671–6687. doi:10.1103/PhysRevB.46.6671.
- ²⁶ J. P. Perdew, K. Burke, M. Ernzerhof, Generalized gradient approximation made simple, *Phys. Rev. Lett.* 77 (1996) 3865–3868. doi:10.1103/PhysRevLett.77.3865.
- ²⁷ P. E. Blöchl, Projector augmented-wave method, *Phys. Rev. B* 50 (1994) 17953–17979. doi:10.1103/PhysRevB.50.17953.
- ²⁸ https://github.com/dalcorso/thermo_pw.
- ²⁹ S. Menon, G. D. Leines, J. Rogal, pycscal: A python module for structural analysis of atomic environments, *J. Open Source Softw.* 4 (43) (2019) 1824. doi:10.21105/joss.01824.
- ³⁰ C. Rycroft, Voro++: A three-dimensional voronoi cell library in c++, Tech. rep., Lawrence Berkeley National Lab.(LBNL), Berkeley, CA (United States) (2009). doi:10.2172/946741.
- ³¹ E. S. Fisher, C. J. Renken, Single-crystal elastic moduli and the hcp \rightarrow bcc transformation in Ti, Zr, and Hf, *Phys. Rev.* 135 (1964) A482–A494. doi:10.1103/PhysRev.135.A482.
- ³² Y. X. Ye, Z. P. Lu, T. G. Nieh, Dislocation nucleation during nanoindentation in a body-centered cubic TiZrHfNb high-entropy alloy, *Scr. Mater.* 130 (2017) 64–68. doi:10.1016/j.scriptamat.2016.11.019.
- ³³ Y. X. Ye, C. Z. Liu, H. Wang, T. G. Nieh, Friction and wear behavior of a single-phase equiatomic TiZrHfNb high-entropy alloy studied using a nanoscratch technique, *Acta Mater.* 147 (2018) 78–89. doi:10.1016/j.actamat.2018.01.014.
- ³⁴ Z. Lei, X. Liu, Y. Wu, H. Wang, S. Jiang, S. Wang, X. Hui, Y. Wu, B. Gault, P. Kontis, et al., Enhanced strength and ductility in a high-entropy alloy via ordered oxygen complexes, *Nature* 563 (7732) (2018) 546–550. doi:10.1038/s41586-018-0685-y.
- ³⁵ L. Zhang, H. Fu, S. Ge, Z. Zhu, H. Li, H. Zhang, A. Wang, H. Zhang, Phase transformations in body-centered cubic Nb_xHfZrTi high-entropy alloys, *Mater. Charact.* 142 (2018) 443–448. doi:10.1016/j.matchar.2018.06.012.
- ³⁶ G. D. Samolyuk, Y. N. Osetsky, G. M. Stocks, J. R. Morris, Role of static displacements in stabilizing body centered cubic high entropy alloys, *Phys. Rev. Lett.* 126 (2021) 025501. doi:10.1103/PhysRevLett.126.025501.
- ³⁷ J. P. Troade, A. Gervois, L. Oger, Statistics of voronoi cells of slightly perturbed face-centered cubic and hexagonal close-packed lattices, *Europhys. Lett.* 42 (2) (1998) 167–172. doi:10.1209/epl/i1998-00224-x.
- ³⁸ P. J. Steinhardt, D. R. Nelson, M. Ronchetti, Bond-orientational order in liquids and glasses, *Phys. Rev. B* 28 (1983) 784–805. doi:10.1103/PhysRevB.28.784.
- ³⁹ W. Lechner, C. Dellago, Accurate determination of crystal structures based on averaged local bond order parameters, *J. Chem. Phys.* 129 (11) (2008) 114707. doi:10.1063/1.2977970.
- ⁴⁰ H. Song, F. Tian, Q.-M. Hu, L. Vitos, Y. Wang, J. Shen, N. Chen, Local lattice distortion in high-entropy alloys, *Phys. Rev. Mater.* 1 (2017) 023404. doi:10.1103/PhysRevMaterials.1.023404.
- ⁴¹ Z. Wang, W. Qiu, Y. Yang, C. Liu, Atomic-size and lattice-distortion effects in newly developed high-entropy alloys with multiple principal elements, *Intermetallics* 64 (2015) 63–69. doi:10.1016/j.intermet.2015.04.014.
- ⁴² D. Ma, B. Grabowski, F. Körmann, J. Neugebauer, D. Raabe, Ab initio thermodynamics of the CoCrFeMnNi high entropy alloy: Importance of entropy contributions beyond the configurational one, *Acta Mater.* 100 (2015) 90–97. doi:10.1016/j.actamat.2015.08.050.